Submitted to ***Engineering Geology*** for possible publication

November 18, 2020

The debris avalanche in Donghekou area triggered by the 2008 Wenchuan (M8.0) earthquake: features and possible transportation mechanisms

Gonghui Wang[1)], Fanyu Zhang[2)], Gen Furuya[3)], Koichi Hayashi[4)], Wei Hu[5)], Mauri McSaveney[5,6)], Runqiu Huang[5)]

Addresses of authors:

1) Gonghui Wang (Corresponding author)
Disaster Prevention Research Institute
Kyoto University
Gokasho, Uji, 611-0011, Japan
Tel: (+81)774-384100; Fax:(+81)774-384105
Email: wang.gonghui.3r@kyoto-u.ac.jp

2) Fanyu Zhang
MOE Key Laboratory of Mechanics on Disaster and Environment in Western China
Department of Geological Engineering
Lanzhou University
Lanzhou 730000, China
Email: Zhangfy@lzu.edu.cn

3) Gen Furuya
Toyama Prefectural University
Kurokawa 5180, Imizu-shi, Toyama 939-0398, Japan
Email: gfuruya@pu-toyama.ac.jp

4) Koichi Hayashi
Geometric Ltd.
San Francisco, California, United States
Email: KHayashi@geometrics.com

5) Wei Hu
State Key Laboratory of Geo-hazard Prevention and Geo-environment Protection
Chengdu University of Technology
Chengdu, Sichuan 610059, P.R. China
Email: 513933225@qq.com

5) Mauri McSaveney
State Key Laboratory of Geo-hazard Prevention and Geo-environment Protection
Chengdu University of Technology
Chengdu, Sichuan 610059, P.R. China
Email: mcsaveney@xtra.co.nz

6) Mauri McSaveney
GNS Science, Lower Hutt, New Zealand
Email: M.McSaveney@gns.cri.nz

5) Runqiu Huang
State Key Laboratory of Geo-hazard Prevention and Geo-environment Protection
Chengdu University of Technology
Chengdu, Sichuan 610059, P.R. China
Email: 706618681@qq.com

The debris avalanche in Donghekou area triggered by the 2008 Wenchuan (M8.0) earthquake: features and possible transportation mechanisms

Gonghui Wang[1)], Fanyu Zhang[2)], Gen Furuya[3)], Koichi Hayashi[4)], Wei Hu[5)], Mauri McSaveney[5,6)], Runqiu Huang[5)]

[1)]Disaster Prevention Research Institute, Kyoto University, Uji, Kyoto, Japan (E-mail: wang.gonghui.3r@kyoto-u.ac.jp; Tel: 81-774384100; Fax: 81-774-384105)

[2)] MOE Key Laboratory of Mechanics on Disaster and Environment in Western China, Department of Geological Engineering, Lanzhou University, Lanzhou 730000, China

[3)] Toyama Prefectural University, Kurokawa 5180, Imizu-shi, Toyama 939-0398, Japan

[4)] Geometric Ltd., San Francisco, California, United States

[5)] State Key Laboratory of Geo-hazard Prevention and Geo-environment Protection, Chengdu University of Technology, Chengdu, P.R. China

[6)] GNS Science, Lower Hutt, New Zealand

ABSTRACT:

In 2008, the Wenchuan earthquake triggered many large landslides with rapid movement and long runouts, resulting in a great number of casualties. Although there have been many studies of the geographical features and initiation mechanisms of some catastrophic landslides, the movement mechanisms for many remain unclear. In this paper, we present a case study of a large landslide (debris avalanche) triggered by the 2008 Wenchuan earthquake in the Donghekou area, Sichuan Province, China. We made detailed field surveys of the geographical features of the landslide and carried out subsurface investigations of the landslide deposits using microtremor array measurement and electrical resistivity tomography (ERT). Based on the observed surficial features, shear-wave velocity (Vs) profiles and 2D electrical resistivity profiles of the landslide deposits, we estimated the possible thickness of landslide deposits at different locations, and also analyzed the possible landsliding mechanisms. We inferred that this landslide resulted from retrogressive failures on the source area, and the displaced landslide materials underwent transitional spreading with further entrainment of debris along the travel path. Multiple mud waves might have been formed in the substrate soil layers along the travel path due to the entraining of landsliding materials, and the landsliding materials might have presented channelized movements, indicating that different parts may have moved at different speeds. This kind of transportation mechanism may provide information for elevating the numerical simulation of landsliding, and also for reuse of deposit area of large landslides.

Keywords: Wenchuan earthquake, debris avalanche, internal structure, landslide deposits, movement mechanism

1. Introduction

Rock or debris avalanches are normally characterized by large volumes, rapid movement and long runouts, and thus are usually catastrophic (e.g., Heim, 1932; McSaveney, 1978; Evans and Clague, 1999; Strom and Adbrakhmatov, 2018). They can be triggered by rainfall, earthquakes, and human activities, and some by unknown factors. To prevent or at least to mitigate the hazards resulting from different types of avalanches, numerous studies had been carried out to better understand their long runout mechanisms (McSaveney et al., 1992; Hungr et al., 2001; Davies and McSaveney, 2002; Hancox et al., 2005; Crosta et al., 2007; Schulz et al., 2008). It has been assumed that the avalanches move as a fluid (e.g. Heim, 1932; Kent, 1966; Hsu, 1975; Voight et al., 1983), as disintegrating rock blocks (McSaveney, 1978), or as sliding blocks riding on thin but ductile basal layers or air cushions (Kent, 1966; Shreve, 1968; Aharonov and Anders, 2006). Statistical data indicate that the mobility of an avalanche is directly related to its volume (Heim, 1932; Scheidegger; 1973), while several physical models, such as fluidization, air cushion, self-lubrication, debris entrainment, dynamic fragmentation, and hydrothermal overpressuring, have been proposed to explain their long runout movement (Kent, 1966; Shreve, 1968; McSaveney, 1978; Davies and McSaveney, 2002; Voight et al., 1983; Anders et al., 2000; Erismann and Abele, 2001; Collins and Melosh, 2003; Goren et al., 2010; Hu et al., 2018). Although these models sound reasonable, most of them are derived from field observation on the surficial features of their deposits with less information on the internal structure of the landslide deposits. This is understandable, because it is normally difficult to conduct detailed surveys on the avalanche deposits with large areas. Nevertheless, understanding the internal structure of the avalanche deposits is important for clarifying the movement mechanism and then validating the suitability of these models mentioned above.

To unravel the internal structure of deposits of debris avalanches, and improve our understanding of long runout movement of displaced materials, we described a debris avalanche triggering by the 2008 Wenchuan earthquake in the Donghekou area (hereinafter termed the Donghekou landslide), Qingchuan County, Sichuan Province, China. Because Donghekou landslide is one of the most catastrophic landslides triggered by the 2008 Wenchuan earthquake and featured by long runout and great number of casualties, immediately after the earthquake, we conducted field survey on the landslide phenomena, investigated the features of the surficial layers of the landslide deposits and examined the shear behavior of landsliding materials for better understanding the possible sliding mechanism (Wang et al., 2014). It is also noted that soon after the earthquake, Donghekou landslide area was designated an earthquake ruins park. This enabled us to conduct further subsurface investigations of the landslide deposits using multiple geophysical approaches, including microtremor array measurement and electrical resistivity topography (ERT). In this paper, we present those newly obtained results. Based on these data we analyze the transportation mechanism of Donghekou landslide, and discuss its implication for understanding the movement mechanisms of other debris avalanches.

2. The 2008 Wenchuan earthquake and Donghekou landslide

The 2008 Wenchuan earthquake (M_w8.3) occurred on 12 May, 2008, at 14:28 local time. The epicenter, with a depth of about 19 km, is in Wenchuan County (Fig. 1) (Huang, 2009), which is 80 km west-northwest of Chengdu City in Sichuan Province, China. The fault rupture resulted in several meters of surface displacements and propagated from the epicenter for about 240 km along the Longmenshan thrust zone. This earthquake caused huge losses in both built infrastructure and human lives. According to the International Strategy for Disaster Reduction (ISDR), more than 87,400 people were confirmed dead, and 459,000 injured (Qi et al., 2010).

More than 60,000 landslides were triggered by the earthquake (Huang and Li, 2009; Dai et al., 2011a; Gorum et al., 2011). The main landslide types include shallow landslides, rock falls, deep-seated landslides, and rock/debris avalanches (Dai et al., 2011b). Although most of the landslides are shallow ones, there were also many catastrophic large landslides, which resulted in severe casualties. One was the Donghekou landslide (Figs. 2 and 3).

The Donghekou landslide is located on the junction zone between Hongguang Town and Guanzhuang Town, Qingchuan County, about 250 km northeast of Chengdu, the capital city of Sichuan Province. It originated from a slope along the confluence of the Qingzhu River and its tributary, the Hongshi River (Fig. 2). The mountains in this area normally reach elevations of more than 1000 m, with an altitude difference (above the river bed) of about 500 m, and have steep upper slopes and gentle lower slopes.

Donghekou landslide is a rockslide-debris avalanche (as defined by Hungr and Evans, 2004) with the runout path material entrained by the impact of rock debris (e.g., Wang et al., 2014; Dai et al., 2011b; Yin et al., 2009, 2011; Xu and Tang, 2009). A bout 1×10^7 m^3 of landslide materials displaced from the source area and descended a vertical distance of about 500 m over a horizontal distance of about 2 km. The landslide material buried the residential areas and the rice paddy on the downstream, and blocked both rivers, resulting in the formation of a dam. It is noted that although the resultant impounding water overflowed a few days late and caused partial collapse of the dam, no further casualties were triggered to the downstream villages due to proper countermeasure.

There were four villages in the Donghekou area before the earthquake. Figs. 3a and 3b present views of the

Donghekou area before and after the earthquake, respectively. There were many houses located on the toe part of the mountains before the earthquake (Fig. 3a). However, almost all these houses were destroyed and the villages buried completely by the displaced landslide materials (Fig. 3b). As a result, about 780 people were killed. The dashed circles (Fig. 3a, b) show the one-story house that survived during the earthquake, while the river shown in Fig. 3b is the breached Qingzhu River.

According to the local geological map (Fig. 4), the exposed strata of the research area consist of Sinian, Cambrian, Silurian and Quaternary systems, and each stratum presents a stripped distribution along the tectonic line. The Sinian system can be divided into three members, i.e., the Third (Zy^3), the Second (Zy^2) and the First (Zy^1) members, based on their age from oldest to most recent. Zy^3 mainly consists of dolomitic limestone, grey blocky dolomite, and dark blocky siliceous dolomite. Zy^2 mainly consists of calcareous sericite phyllite, thin layer of crystalline limestone, and lenticular dolomite. Zy^1 mainly consists of siliceous banded dolomite and siliceous dolomite. The Cambrian system consists of the Youfang Formation (€y) and Qiujiahe Formation (€q). €y mainly consists of calcareous tuffaceous sandstone, and tuffaceous sericite phyllite; while €q consists of carbonaceous siliceous slate and siliceous rock, with low-grade Mn ore. The Quaternary strata (Q_h) are mainly distributed in the valley of the landslide deposit area, and consisted of alluvial or alluvial deposits (riverbed sand, gravel, silt and clay) of the Holocene Series. The lithology changes greatly, and the thickness of the siliceous dolomite interlayer is also different. The bottom is a carbonaceous siliceous slate sandwiched with thin layer of siliceous dolomite, partially lumpy siliceous dolomite. The Sinian system mainly crops out on the middle-upper part of the landslide slope, and the Donghekou landslide originated mainly in this stratum. The Cambrian Youfang and Qiujiahe Formations are found on the right side of the landslide body and the middle and lower part of the slope body. A fault (Hongkan Fault) passing through the source area has been identified (Xu and Tang, 2009; Yu et al., 2010; among others). Large extension cracks had been identified to the left side of the source area before the earthquake, and the residents were made aware of slope instability, so evacuation was enforced during heavy rainfall events.

As reported by Wang et al (2014), six months after the earthquake, fumaroles with sulfur smell appeared on the middle part of the landslide (as shown in Fig. 5). Wang et al. (2014) carried out long-term monitoring of the ground temperature around the fumarole opening and reported that the ground temperature was measured as 65°C in highest value. They also conducted chemical analyses of the liquid and gas collected from the vents of the fumaroles, and concluded that the fumaroles resulted from the weathering of underlying landslide materials and bedrock (carbonaceous siliceous slate).

3. Methods

To unravel the internal structure of the landslide deposits, Wang et al (2014) measured the 2D shear-wave velocity (V_s) profile of the landslide deposits by using the active multichannel analysis of surface waves (MASW) method. Details for the principles of MASW method can be referred to Park et al. (1998), Miller et al. (1999), Hayashi and Suzuki (2004), and Hayashi et al. (2008). Due to the limitation in the surveying depth (usually in the range of 10-20 m) through this active MASW method, Wang et al (2014) failed to obtain the Vs information for the layers of the landslide deposits deeper than 20 m, such that the formation of the sliding surface remains unclear. Therefore, in this study we employed a passive MASW method (microtremor array measurement) (Park et al., 2005), in which ten geophones with a natural frequency of 2 Hz for each were placed in an equilateral triangle (as illustrated in Fig. 6). According to Okada (2003), the detection depth through this kind of observation array for the passive MASW method is practically about three to four times of the observation radius (the distance between G2 and G11 as shown in Fig. 6). Therefore, by employing the observation array shown in Fig. 6, a detection depth of about 80 m beneath the central point (G2) of the triangle could be expected. It is noted that in both the active and passive MASW methods, we employed the instrument of McSEIS-SXW (OYO Corporation) for data acquisition, and used SeisImager/SW software (OYO Corporation) for the raw data process and analysis.

Passive MASW surveys were carried out at two locations (M1 and M2 in Fig. 7) on the landslide deposit area in the early morning (around 5:00 AM) of November 22, 2009, to avoid strong anthropogenic noise from cars, trucks, and other machines. At each location, altogether 27 records were measured without changing the geophone array, and each record was sampled at a frequency of 500 Hz with a data length of 16384. It is noted that Wang et al (2014) conducted active MASW survey along three survey lines on the landslide deposit area, and their locations (L1-L3) are also presented in Fig. 7. Fig. 8 shows an example of one record acquired at location M2. Using the SeisImager/SW software, a file list was at first constructed by reading all the 27 records acquired by the McSEIS-SXW, which was followed by the setup of array geometry and calculation of 2D spatial autocorrelation. Thereafter, a phase velocity image in frequency domain was obtained through the phase velocity-frequency transformation in which a maximum velocity and a maximum frequency were set as 1000 m/s and 16 Hz, respectively. Basing on the phase velocity image, phase velocities were picked automatically at the mathematical maximum amplitude for each frequency by setting up the minimum frequency as 2 Hz. Because the passive MASW data do not include shallow depth information (less than 5~10 m), we used the active data that were obtained along L3 and presented in Wang et al (2014) through location projection, and conducted similar analyses to get the phase velocity image. Based on these phase velocity images, the dispersion curve was extracted. Based on the dispersion curve, an initial model for the 1-D shear wave velocity (Vs) profile was constructed by simple depth transformation, which includes calculating the wavelength (λ) from frequency and phase-velocity, inferring the depth that is defined as λ/3, and plotting the phase-velocity on depth-velocity chart. Finally, the 1-D shear wave velocity (Vs) profile was estimated by fitting the observed and the theoretical phase velocities through inversion. It is noted that non-linear least square method was employed in the inversion with number of iterations = 5, scaling factor = 0.15, acceleration factor = 2.0, and damping factor = 0.01. More details on the data acquisition and analysis for both the active and passive surface wave methods could be obtained in SeisImager/SW^{TM} Manual (Geometrics, Inc., 2009).

We also used Electrical Resistivity Tomography (ERT) to measure the 2D images of the distribution of electrical resistivity in the landslide deposits. ERT surveys enable identification of resistivity contrasts that may result from both the lithological nature of the deposits and variation in water content. Due to its effectiveness, ERT had been widely used in landslide studies (Perrone et al., 2014).

An ERT survey was conducted in March 2018, in which measurements were carried out using the Wenner method. All ERT data were processed using 2D inversion with the RES2Dinv software, which is based on a technique proposed by Loke and Barker (1996). Three lines (E3-E5) were arranged along the transverse direction of the deposit area, while two lines (E1 and E2) were individually set along the longitudinal direction, due to the spillway along Hongshi River. The locations of ERT survey lines E1-E5 are superimposed in Fig. 7, where a zoomed view (based on the Google Earth image shot on October 30, 2019) of the window shown in Fig. 2a is used.

4. Results

4.1 Shear velocity profile

The analyzed results obtained from the measurements at M2 are summarized in Fig. 9, where Figs. 9a and 9b present the phase velocity images in frequency domain obtained from active and positive MASW methods, respectively. The dispersion curve extracted from Fig. 9a (for the data with frequency being ranging from 8~40 Hz) and 9b (for the data with frequency being less than 8 Hz) is depicted in Fig. 9c, where wavelengths calculated from the phase velocity and frequency are also presented. Fig. 9d plots the inverted 1-D Vs profile together with the original picked phase velocities (presented by red points) whose depths were estimated following the one-third-wavelength approximation. In Figs. 9a and 9b, the error between the observed coherences and the theoretical Bessel functions is displayed by different colors: magenta indicates large error and blue presents small error. The red dots indicating the phase velocities with minimum-error at each frequency are picked for the construction of observed dispersion curves, and plotted in Fig. 9c. The observed dispersion curve shown in Fig. 9c enabled the analysis of V_s to a depth of about 80 m (as shown in Fig. 9d). In Fig. 9d, the darker grey marks the valid range of the inversion, while the light grey is not based on data. From Fig. 9d, it is seen that the V_s for the surficial layer (0~5.4 m in depth) is less than 230 m/s, and increases to 270 m/s approximately for the layer in the depth of 5.4 ~ 12.3 m. The soil layers between the depth of 12.3 m and 20.8 m have their V_s being 440~590 m/s approximately, while all the soil layers deeper than 20.8 m show Vs values greater than 700 m/s.

Fig. 10 presents the phase-velocity images in frequency domain, dispersion curve and the 1-D Vs profile for the measurements at M1. Similar to M2, both the active and passive data show clear dispersion curve, and enable the analysis of Vs to a depth of about 73 m. However, it is worth noting that at M1, Vs shows a sharp change from 426 m/s to 700 m/s approximately at the depth of 25.6 m. After that, Vs increases to 740 m/s at the depth of 36.3 m and further to 810 m/s at the depth of 42.3 m, and finally does not show remarkable change with further increase of depth.

4.2 ERT profile

Figs. 11a and 11b show the electrical resistivity tomographies measured along the E1 and E2 survey lines, respectively. In Fig. 11a, the domain in the upper stream area (zone D4) and surficial soil layers (0 – 10 m deep) show high resistivity (>255 ohm·m) in general, with an exception for the surficial layer ranging from 255 m to 305 m along the profile; there the resistivities are smaller than 150 ohm·m. Three zones (D1, D2 and D3) show remarkably low resistivities. In zone D1 the resistivities range from about 16–25 ohm·m; while the resistivities in D2 and D3 are <15 ohm·m.

In Fig. 11b, the surficial soil layers upstream of survey line E2 (10 ~ 210 m) have a high resistivity (>255 ohm·m), while downstream they show relatively low resistivity. Underneath the surficial soil layer, the resistivity lowers to a small value (about 8 ohm·m at a minimum) in most area. However, the resistivity increased with further increases of depth, presenting a clear contrast with the two clusters of high resistivities. It is also noticed that the domain (D5) located between 170–200 m in HD and at 630–590 m in elevation shows lower resistivities (< 127 ohm.m).

Figure 12 presents the electrical resistivity tomographies measured along the E3, E4 and E5 lines, respectively. Due to a limitation on available survey cable lengths, the span of survey Lines E3 and E4 are less than 140 m, while E5 spanned 295 m. In all the survey lines, the start (zero) point indicates the right margin (looking downslope) of the landslide deposits. In Line E5 (Fig. 12a), the surficial layer (about 10 m thick) shows higher resistivities, except for the domain of 100 ~135 m in horizontal distance, while the deeper domains showed clear contrasts in resistivity structure, and the zone having approximately the same values in resistivity inclined leftward with increase of depth in general. For the survey line E4 (Fig. 12b), the surficial layer (about 6 m deep) shows high resistivity, and underneath the surficial layer there are several separated domains with low resistivity, and these domains are approximately horizontal. In Fig. 12b, it can be seen that some of the domains are underlain by layers with higher resistivity. The surficial layer in survey line E3 (Fig. 12c) does not show distinguishable contrast within the deeper soil layer. However, a domain of relatively high resistivities located at the surficial distance of 40–45 m inclined rightward with increase of depth, while another domain (starting from 95 to 105 m on the surficial layer) inclined leftward with increase of depth, and the area between these two domains presents low resistivities.

5. Discussion

By now, several interpretations have been proposed to explain the long runout movement of Donghekou landslide (Xu and Tang, 2009; Yin et al., 2009, 2011; Wang, et al., 2014). Some studies emphasized the effect of strong seismic motion on the possible sliding velocity of landslide materials when they slid from the source area (Zhou et al., 2013; Zhang et al., 2015), while others examined the effect of entrainment of debris on the mobility along the transport path (Yuan et al., 2014; Wang et al., 2014).

Numerical simulations using different approaches have been carried out to simulate the processes of transportation and deposition of landslide materials (Li et al., 2012; Zhang et al., 2013, 2015; Huang et al., 2012a, among others). For example, Li et al. (2012) simulated the kinematic behavior and concluded that a low friction coefficient (about 0.1) is required to justify its mobility. Yuan et al. (2014), using 2-D DEM analysis, concluded that the landslide in the source area began as a push-type and then changed to a retrogressive one, and the entrainment of sliding path materials slightly elevated the mobility. Zhang et al. (2015) analyzed the mobility of the Donghekou landslide using a seismic discontinuous deformation analysis (DDA) approach and concluded that seismic loading on the displaced landslide materials could be a factor helping increase the mobility of the Donghekou landslide. Huang et al. (2012b) concluded that Donghekou landslide may have several flow stages with long sliding distances. Nevertheless, most of these studies are based on surficial examination of the landslide deposits without information on their internal structure. As pointed out by Strom (2006), developing reliable models for predicting the movement and deposition processes of a landslide mass needs to intercorporate the topographical, structural and depositional features, which should be regarded as constraints for checking the reliability of the numerical model. However, for Donghekou landslide, the internal features of the landslide deposits and the basal sliding surface have not been clarified, so that the numerical simulations can only use the deposit area of the landslide materials as the constraint for model calibration. This may be the reason why different failure models for the landslide materials from the crown were adopted in different simulations.

The thickness of the landslide deposits on Donghekou area seems to be an unsolved issue. For example, the descriptive texts on some guide plates erected on the ruins park tell indicate that some areas of the landslide deposits damming these rivers have a thickness of more than 100 m. On the other hand, Zhang et al (2011) reported that the thickness of the landslide deposits varies from several meters to dozens of meters, while Xu and Tang (2009) reported that the landslide dams on Hongshi River and Qingzhu River are about 50 m and 20 m in height, respectively. Further, Li et al (2012) stated that the landslide dam on Qingzhu River is about 25 m in maximum thickness. From Figs. 10d, it is noticed that V_s of the soil layer changes from 460 m/s to 700 m/s at the depth of about 25.6 m. Considering that V_s = 700 m/s had been widely used for defining the engineering bedrock (Miller et al., 1999; Santamarina et al., 2001), we infer that the soil layer deeper than 25.6 m with V_s > 700 m/s be the bedrock of the original ground, and the overlaid soil layers be the landslide deposits, and then the landslide deposits at location M1 may have a thickness of about 25.6 m. This inference is supported by the ERT results shown in Fig. 11d, where the electrical resistivities of soil layers show significant contrast at the depth of about 26 m. By comparing Figs. 9d and 11b, we further infer that the thickness of landslide deposits at location M2 be about 21 m. It is noted that these inferred thicknesses show good consistency with the maximum thickness of 25 m reported by Li et al (2012), although they did not provide any evidence for the estimation of this value. In this sense, our result for the possible thickness of landslide deposits provides reliable evidence, because previous estimates for the thickness of the landslide deposits in the Donghekou area were based on a DEM with a 10-m-contour, which was the only available one for this area before the earthquake.

According to Dunning and Armitage (2011), rock-avalanche deposits commonly have three sedimentary facies: a carapace facies, a body facies, and a basal facies. The carapace facies represents the coarsest unit composing the surface and near surface, the body facies is the main body of the rock-avalanche deposit, while the basal facies indicates the base of the rock-avalanche deposit. By employing the active MASW method, Wang et al. (2013b) examined V_s values of the deposits of a landslide that was triggered by the same earthquake in the Tianchi area, Sichuan. They identify a clear boundary between the basal facies and the body facies, and suggest that the superficial layer (carapace facies) and the bottom layer (basal facies with a thickness of about 2-3 m) have relatively smaller shear-wave velocities.

For Donghekou landslide, Wang et al (2014) conducted active MASW survey along three survey lines (L1-L3) on the landslide deposit area. Fig.13 summarizes the Vs profiles along these survey lines. As reported in Wang et al (2014), L1 and L2 are laid along the drainage channel on the right and left banks, respectively, and are 70 m apart. The Vs profile along L2 (Fig. 13a) showed that the upper layers are weaker, with V_s values ranging from 250–300 m/s. This weak layer is about 12 m thick near the zero point at the horizontal distance (HD) and becomes thicker when the HD becomes greater. For L1, the upper weaker layers with V_s values ranging from 250–300 m/s are thin and their thickness increases also when HD becomes greater (Fig. 13b). The shear-wave velocity along L3 showed that the superficial soil layers have small V_s values (ranging from 180–270 m/s) (Fig. 13c). From Figs. 9, 10 and 13, it is inferred that the most upper layers of landslide deposits with small Vs values may present the carapace facies. The existence of carapace facies can also be inferred from the ERT profile shown in Fig. 11. The vertical distribution of resistivity at Location M2 (shown in Fig. 11b) indicates the existence of three main layers, namely, surficial layer (about 5 m thick) with resistivity being greater than 100 ohm.m, middle layer (about 10 m thick) with the resistivity being among 60~100 ohm.m, and the bottom layer locating above the dashed line (about 4 m thick) with resistivity being among 100-127. It is understood that the resistivity of a soil layer could be changed with variation of soil moisture. However, the high resistivities in Fig. 11b are distributed along the superficial layers at different elevation (say from 0 to 200 m in HD), it will be reasonable to infer that the high resistivity of the superficial layers results from loose soil structure, which may result in small Vs value, corresponding to the carapace facies.

It is also noted that the basal facies consisting of thin layers with smaller Vs values had not been identified through these V_s profiles presented in Figs. 9, 10 and 13, probably because the basal faces is located in a depth to which the active MASW method failed to reach, while the basal faces is too thin such that the passive MASW method failed to individuate it, i.e., the thickness of the basal faces is out of the resolution of the passive MASW method. Therefore, further survey, such as drilling, will be necessary to delineate the basal facies in the landslide deposits of Donghekou area.

As pointed out by Hungr et al. (2001), in debris avalanches, multiple surges are not common, but may occur as a result of retrogressive failures from the crown or slides off the source scar. The ERT results (Fig. 11a) indicate the presences of several domains with diagonally forward isopleth resistivity. This phenomenon might result from progressive failures occurring on the source area. As reported by Wang et al. (2014), the colluvium in the valley on area B1 (Fig. 3) started its movement almost at the same time as the landsliding originating on the upper slope (area B2), which was followed by the downslope movement of the “mountain” on area B3. Further failures on a smaller scale on the source area continued for two days. Zones D2 and D3 (Fig. 11a) mainly consist of slate rocks, where rapid chemical weathering (biological oxidation of pyrite) caused the appearance of fumes (as shown in Fig. 5) and resulted in an increase in ground temperature for some years after the earthquake (Wang et al., 2014). The domain with high resistivity upstream of D4 may present the deposits of fragmented dolomite limestone originating from the uppermost source area.

Landslide materials originating from a source area often may entrain debris along the sliding path, increasing the landslide mobility and destructiveness (Sassa, 1985; Hungr and Evans, 2004; McDougall and Hungr, 2005; Wang et al., 2003, 2013a, 2014; Crosta et al., 2009; Mangeney et al., 2010; Berger et al., 2011; Dufresne, 2012; Zhou et al., 2016). Although entrainment has also been incorporated in some numerical landslide simulations, the interaction between the sliding debris and the original ground along the sliding path remains unclear. Hungr and Evans (2004) presented a hypothetical mechanism of a flow with entrainment of liquefiable materials and provided a schematic illustration for the interaction between the moving rock mass and the substrate along the travel path (Fig. 14). In this model, the landsliding materials from the source area may trigger liquefaction through impact on a liquefiable substrate layer (Fig. 14b). As the result, a mud wave could be formed and then projected forward (Fig. 14c), and finally the rock mass may be deposited on the mud wave with long travel (Fig. 14d). For the Donghekou landslide, the electrical resistivity topography profiles presented in Fig. 11b suggest that the landsliding of those long-traveled materials might have involved multiple surges resulting from different failure stages. The contour lines (dashed lines) for the resistivities of 127–200 ohm.m in the domain starting from HD 75 to 135 m are approximately horizontal, and then shift to an uphill inclination with further increase in HD (from HD 135 to 170 m). A similar phenomenon can be observed for the domain from HD 200 to 310 m. As mentioned above, we infer that the soil layers underneath the soil layer (with resistivities of 127–200 ohm.m) are the former ground surface before the earthquake, and the ground underwent shear failures at different locations along the travel path during the landsliding, resulting in the formation of multiple mud waves, as shown in Fig. 11.

Through comparing the V_s profile along L2 and the ERT profile along E5 (Fig. 15), we found that channelized sliding may also have occurred within the landsliding materials during the emplacement. As shown in Fig. 15a, the boundaries showing greater V_s values (marked by dashed lines at points of P and P’) are approximately in good agreement with those revealed by the ERT profile (as presented by points of Y and Y’ in Fig. 15b). Similar phenomena can also be identified in the ERT profile shown in Fig. 12c, where the locations of the boundaries are marked by R and R’, and in the Vs profiles shown in Figs.13a and b (locations are marked by T and T’). We interpret these boundaries as longitudinal ridges, which channelized the emplacement of sliding material. As pointed out in other studies, longitudinal ridges are a frequently occurring topographical feature on rock avalanches deposits (Dufresne and Davies, 2009; Dufresne et al., 2010, 2019; Dunning et al., 2015; Shugar and Clague, 2011), and could be in the form of ridges, flowbands or aligned hummocks that are characterized by differences in texture. Although shearing within the moving debris has been inferred as one reason for these kinds of ridges or flowbands, details on their formation remain unclear (Dufresne et al., 2019). Therefore, the V_s and ERT profiles (Figs. 12 and 15) provide evidence for better understanding the internal structures of these ridges or flowbands.

The lower resistivities (< 127 ohm.m) in the domain D5 shown in Fig. 11b may suggest the existence of a fault that had not been identified yet. Based on the topography and location of an old landslide located on the slope on the right side of the landslide deposit area, we infer that a fault (see Fig. 7) may exist. Nevertheless, concerning this inference, further surveys will be necessary and will be conducted in the near future.

6. Conclusions

During the 2008 Wenchuan earthquake (M8.0), a catastrophic landslide occurred in the Donghekou area. The landslide had a total volume of about 1×10^7 m^3 and a travel distance of about 2.0 km, with an elevation drop of about 500 m. Four villages were buried by the landslide materials, and more than 780 people were killed. The displaced landslide materials also dammed two rivers, threatening people downstream immediately after the earthquake. Field investigations and geophysical surveys using different approaches suggest the following conclusions.

1. Donghekou landslide can be classified as a debris avalanche. The landslide materials originating from the source area involved retrogressive failures, resulting in the formation of a landslide deposit with differing internal structures at different locations.
2. The landslide materials deposited in the upper stream area of the valley (immediately below the toe of the landslide slope) showed complex structures. Two domains showed very low resistivities, representing deposits of slate rocks from the landslide source area and weathered quickly after being outcropped.
3. Combined analyses of both passive and active surface waves enabled the pickup of dispersion curve in an extended frequency range, and then enabled the estimation of Vs for the soil layers to a depth of about 80 m. The Vs and ERT profiles provided more reliable evidence for estimating the thickness of landslide deposits, and also provided information for understanding the carapace facies formed in the landslide deposits.
4. The ERT profiles suggest that the landsliding materials may have involved at least two main surges, which resulted in the formation of mud waves in the substrate soil layers along the slide path.

5. The V_s and ERT profiles along lines traversing the landslide deposits reveal that channelized sliding may have occurred within the landsliding materials. The structure of the channelized sliding provides evidence for understanding the formation of ridges within landslide materials during their emplacement.

Finally, it is noted that all these inferences mentioned above are based on the MASW and ERT data. Considering the limitation of these geophysical survey methods, further survey (such as borehole drilling) will be needed to elevate the accuracy of these inferences. Applying these methods to some landslides in Japan are also in operation for better understanding the internal structures of landslide deposits resulting from different types of landslides triggered by rainfall and/or earthquake.

Acknowledgement

This research was supported by the Open Fund of the State Key Laboratory of Geohazard Prevention and Geoenvironment Protection (Chengdu University of Technology) (Nos. GZ2009-02 and SKLGP2018K006), scientific research grants from the MEXT of Japan (Grant No. 18380094, 19310124, and 19KK0121), and International Collaborative Research (2020W-01) funded by the Disaster Prevention Research Institute, Kyoto University. We thank Prof. Oliver Korup in Potsdam University, Dr. Johannes Weidinger in Erkudok Institute/Museum of Gmunden, and Dr. Chris Massey in GNS Sciences, New Zealand, for their valuable discussions in the field trips to this landslide; Dr. Issei Doi at Disaster Prevention Research Institute, Kyoto University, for his valuable discussion in the Microtremor analysis; Mr. Yongqing Liu, Mr. Xishan Lin, and Mr. Hailin An, for their help in the ERT survey; Mr. Xianggui He for his logistical help in the field work. Valuable English editing by Dr. Eileen McSaveney (GNS Science, New Zealand) is appreciated. Finally, the editor-in-chief, Dr. Janusz Wasowski, and two reviewers of this paper are greatly thanked for their valuable comments that led to substantial improvement of this paper.

References

Aaron, J., McDougall, S., 2019. Rock avalanche mobility: The role of path material. Engineering Geology 257, 105126.

Aharonov, E., Anders, M.H., 2006. Hot water: a solution to the Heart Mountain detachment problem. Geology 34, 165–168.

Anders, M.H., Aharonov, E., Walsh J.J., 2000. Stratified granular media beneath large slide blocks: implications for mode of emplacement. Geology 28, 971–974.

Berger, C., McArdell, B.W., Schlunegger, F., 2011. Direct measurement of channel erosion by debris flows,

Illgraben, Switzerland. Journal of Geophysical Research 116(F1), pp. 93–104.
Collins, G.S., Melosh, H.J., 2003. Acoustic fluidization and the extraordinary mobility of sturzstroms. J. Geophys. Res. 108 (B10), 2473.
Crosta, G.B., Frattini, P., Fusi, N., 2007. Fragmentation in the Val Pola rock avalanche, Italian Alps. J. Geophys. Res. 112, F01006.
Crosta, G.B., Imposimato, S., Roddeman, D., 2009. Numerical modelling of entrainment/deposition in rock and debris-avalanches. Engineering Geology 109(1-2), 135–145.
Dai, F.C., Tu, X.B., Xu, C., Gong, Q.M., Yao, X., 2011b. Rock avalanches triggered by oblique-thrusting during the 12 May 2008 Ms 8.0 Wenchuan earthquake, China. Geomorphology 132(3-4), 300–318.
Dai, F.C., Xu, C., Yao, X., Xu, L., Tu, X.B., Gong, Q.M., 2011a. Spatial distribution of landslides triggered by the 2008 Ms 8.0 Wenchuan earthquake, China. Journal of Asian Earth Sciences 40, 883–895.
Davies, T.R., McSaveney, M.J., 2002. Dynamic simulation of the motion of fragmenting rock avalanches. Canadian Geotechnical Journal 39(4), 789–798.
Dufresne, A., 2012. Granular flow experiments on the interaction with stationary runout path materials and comparison to rock avalanche events. Earth Surface Processes and Landforms 37(14), 1527–1541.
Dufresne, A., Davies, T.R., 2009. Longitudinal ridges in mass movement deposits. Geomorphology 105:171–181
Dufresne, A., Davies, T.R., McSaveney, M.J., 2010. Influence of runout-path material on emplacement of the round top rock avalanche, New Zealand. Earth Surface Processes and Landforms 35, 190-201.
Dufresne, A., Wolken, G.J., Hibert C., Bessette-Kirton, E. K., Coe, J.A., Geertsema, M., Ekström, G., 2019. The 2016 Lamplugh rock avalanche, Alaska: deposit structures and emplacement dynamics. Landslides 16, 2301–2319.
Dunning, S.A., Almitage, P.J., 2011. The grain-size distribution of rock-avalanche deposits: implication for natural dam stability. In: Evans, S.G., Hermanns, R., Scarascia-Mugnozza, G., Strom, A.L. (eds), Natural and Artificial Rockslide dams, 133. Lecture Notes in Earth Sciences, pp.479–498.
Dunning, S.A., Rosser, N.J., McColl, S.T., Reznichenko, N.V., 2015. Rapid sequestration of rock avalanche deposits within glaciers. Nature Communications 6(7964), 7
Erismann, T.H., Abele G., 2001. Dynamics of Rockslides and Rockfalls. 3-540-67198-6, Springer-Verlag, Berlin, Heidelberg, 316 pp.
Evans, S.G., Clague, J.J., 1999. Rock avalanches on glaciers in the Coast and St. Elias Mountains, British Columbia. In: Proceedings of the 13th Annual Vancouver Geotechnical Society Symposium, Vancouver, pp. 115–123.
Geometrics, Inc., 2009. SeisImager/SW™ Manual. 314p. https://geometrics.com/wp-content/uploads/2019/04/SeisImagerSW_Manual_v3.0.pdf (accessed on September 15, 2020)
Goren, L., Aharonov, R., Anders M.H., 2010. The long runout of the Heart Mountain landslide: heating, pressurization, and carbonate decomposition. J. Geophys. Res., Solid Earth 115 (B10), Article B10210.
Gorum, T., Fan, X.M., van Westen, C.J., Huang, R.Q., Xu, Q., Tang, C., Wang, G., 2011. Distribution pattern of earthquake-induced landslides triggered by the 12 May 2008 Wenchuan earthquake. Geomorphology 133(3-4), 152–167.
Hancox, G.T., McSaveney, M.J., Manville, V.R., Davies, T.R., 2005. The October 1999 Mt Adams rock avalanche and subsequent landslide dam-break flood and effects in Poerua River, Westland, New Zealand. New Zealand

Journal of Geology and Geophysics 48(4), 683–705.

Hayashi, K., Hirade, T., Iiba, M., Inazaki, T., Takahashi. H., 2008. Site investigation by surface-wave method and micro-tremor array measurements at central Anamizu, Ishikawa Prefecture. Butsuri-Tansa (Geophys. Explor.) 61, 483–498 (in Japanese with English abstract).

Hayashi, K., Suzuki, H., 2004. CMP cross-correlation analysis of multi-channel surface-wave data. Exploration Geophysics 35, 7–13.

Heim, A., 1932. Bergsturz und Menschenleben. Fretz and Wasmuth, Zurich. 218 pp.

Hsu, K.J., 1975. Catastrophic debris streams (Sturzstroms) generated by rockfalls. Geol. Soc. Am. Bull. 86, 129–140

Hu, W., Huang, R.Q., McSaveney, M., Zhang, X.H., Yao, L., Shimamoto, T., 2018. Mineral changes quantify frictional heating during a large low-friction landslide. Geology 46 (3), 223–226.

Huang, R.Q., 2009. Geohazard assessment of the Wenchuan Earthquake. Science Press, 944P (in Chinese).

Huang, R.Q., Li, W.L., 2009. Analysis of the geo-hazards triggered by the 12 May 2008 Wenchuan Earthquake, China. Bulletin of Engineering Geology and the Environment 68, 363–371.

Huang, R.Q., Pei, X.J., Fan, X.M., Zhang, W.F., Li, S.G., Li B.L., 2012. The characteristics and failure mechanism of the largest landslide triggered by the Wenchuan earthquake, May 12, 2008, China. Landslides 9(1), 131–142.

Huang, Y., Zhang W.J., Xu, Q., Xie, P., Hao, L., 2012b. Run-out analysis of flow-like landslides triggered by the Ms 8.0 2008 Wenchuan earthquake using smoothed particle hydrodynamics. Landslides 9, 275–283.

Hungr, O., Evans, S.G., 2004. Entrainment of debris in rock avalanches: An analysis of a long run-out mechanism. Geological Society of America Bulletin 116(9), 1240–1252.

Hungr, O., Evans, S.G., Bovis, M.J., Hutchinson, J.N., 2001. A review of the classification of landslides of the flow type. Environmental & Engineering Geoscience 7(3), 221–238.

Kent, P.E., 1966. The transport mechanism in catastrophic rock falls. J. Geol., 74 (1966), pp. 79–83.

Li, X.P., He, S.M.., Luo, Y., Wu Y., 2012. Simulation of the sliding process of Donghekou landslide triggered by the Wenchuan earthquake using a distinct element method. Environmental Earth Sciences 65: 1049–1054.

Loke, M.H., Barker, R.D., 1996. Rapid least-squares inversion of apparent resistivity pseudo-sections using quasi-Newton method. Geophysical Prospecting 48, 181–152.

Mangeney, A., Roche, O., Hungr, O., Mangold, N., Faccanoni, G., Lucas, A., (2010. Erosion and mobility in granular collapse over sloping beds. Journal of Geophysical Research 115(F3), 1–21.

McDougall, S., Hungr, O., 2005. Dynamic modelling of entrainment in rapid landslide. Canadian Geotechnical Journal 42(5), 1437–1448.

McSaveney, M.J., 1978. Sherman Glacier rock avalanche, Alaska, USA. B. Voight (Ed.), Rockslides and Avalanche, Elsevier, Amsterdam, Netherlands. pp. 197–258.

McSaveney, M.J., Chinn, T.J., Hancox, G.T., 1992. Rock Avalanches of 14 December 1991, New Zealand. Landslide News 6, 32–34.

Miller, R.D., Xia, J., Park, C.B., Ivanov, J.M., 1999. Multichannel analysis of surface waves to map bedrock. The Leading Edge 18, 1392–1396.

Okada, H., 2003. The Microtremor Survey Method, Geophysical Monograph, Vol. 12, Society of Exploration Geophysicists, Tulsa, OK.

Park, C.B., Miller, R.D., Ryden, N., Xia, J., Ivanov, J., 2005. Combined use of active and passive surface waves. Journal of Environmental and Engineering Geophysics 10, 323–334.

Park, C.B., Miller, R.D., Xia, J., 1998. Imaging dispersion curves of surface waves on multi-channel record. 68th Annual International Meeting, SEG, Expanded Abstracts, 1377–1380.

Perrone, A., Lapenna, V., Piscitelli, S., 2014. Electrical resistivity tomography technique for landslide investigation – A review. Earth-Science Reviews 135, 65–82.

Qi, S.W., Xu, Q., Lan, H.X., Zhang, B., Liu, J.Y., 2010. Spatial distribution analysis of landslides triggered by 2008.5.12 Wenchuan Earthquake, China. Engineering Geology 116(1–2), 95–108.

Santamarina, J.C., Klein, K.A., Fam, M.A., 2001. Soil and Waves. John Wiley & Sons Inc, New York.

Sassa, K. (1985). The mechanism of debris flows. In: Proceeding of the XI International Conference on Soil Mechanics and Foundation Engineering, San Francisco, pp. 1173–1176.

Schulz, W.H., Harp, E.L., Jibson, R.W., 2008. Characteristics of large rock avalanches triggered by the November 3, 2002 Denali Fault earthquake, Alaska, USA. Proceedings of 10th International Symposium on Landslides and Engineered Slopes, Xi'an, China, June 30 ~ July 4, 2008

Sheidegger, A.E., 1973. On the prediction of the reach and velocity of catastrophic landslides. Rock Mechanics 5, 231-236.

Shreve, R.L., 1968. Leakage and fluidization in air-layer lubricated avalanches. Geol. Soc. Am. Bull. 79 (5), 653–658.

Shugar, D.H., Clague, J.J., 2011. The sedimentology and geomorphology of rock avalanche deposits on glaciers. SLAS Faculty Publication, 336, 44 p.

Strom, A.L., 2006. Morphology and internal structure of rockslides and rock avalanches: grounds and constraints for their modelling. In: Evans, S.G., Scarascia Mugnozza, G., Strom, A., Hermanns, R.L. (eds), Landslides from Massive Rock Slope Failure. NATO Science Series: IV: Earth and Environmental Sciences 49, 305–328.

Strom, A., Abdrakhmatov, K. (2018). Rockslides and rock avalanches of Central Asia. Elsevier, 449p.

Tang, C., Zhu, J., Qi, X., Ding, J., 2011. Landslides induced by the Wenchuan earthquake and the subsequent strong rainfall event: A case study in the Beichuan area of China. *Engineering Geology* 122(1-2): 22–33.

Voight, B., Janda, R.J., Glicken, H., Douglass, P.M., 1983. Nature and mechanics of the Mount St. Helens rock slide-avalanche of 18 May 1980. Géotechnique 33, 243–273.

Wang, G., Huang, R.Q., Chigira, M., Wu, X.Y., Lourenço S.D.N., 2013a. Landslide amplification by liquefaction of runout path material after the 2008 Wenchuan (M8.0) earthquake, China. Earth Surface Processes and Landforms 38, 265–274.

Wang, G., Huang, R.Q., Kamai, T., Zhang F.Y., 2013b. The internal structure of a rockslide dam induced by the 2008 Wenchuan (M_w7.9) earthquake, China. Engineering Geology 156, 28–36.

Wang, G., Huang, R.Q., Lourenço, S.D.N., Kamai, T., 2014. A large landslide triggered by the 2008 Wenchuan (M8.0) earthquake in Donghekou area: phenomena and mechanisms. Engineering Geology 182(Part B), 148–157.

Wang, G., Sassa, K., Fukuoka, H., 2003. Downslope volume enlargement of a debris slide-debris flow in the 1999 Hiroshima, Japan, rainstorm. Engineering Geology 69(3-4), 309–330.

Xu, Q., Tang, M.G., 2009. Donghekou landslide, Qingchuan. In (Xu *et al*. eds): Large-scale landslides induced by the Wenchuan Earthquake, Science Press, Beijing, pp 221–263

Yin, Y.P., 2008. Researches on the Geo-hazards triggered by Wenchuan Earthquake, Sichuan. Journal of Engineering Geology 16, 433–444 (in Chinese).

Yin, Y.P., Wang, F.W., Sun, P., 2009. Landslide hazards triggered by the 2008 Wenchuan earthquake, Sichuan, China. Landslides 6(2), 139–152.

Yin, Y.P., Zheng, W.M., Li, X.C., Sun, P., Li, B., 2011. Catastrophic landslides associated with the M8.0 Wenchuan earthquake. Bulletin of Engineering Geology and the Environment 70, 15–32.

Yu, G.H., Xu, X.W., Klinger, Y., Diao, G.L., Chen, G.H., Feng, X.D., Li, C.X., Zhu, A.L., Yuan, R.M., Guo, T.T., Sun, X.Z., Tan, X.B., An, Y.F., 2010. Fault-Scarp Features and Cascading-Rupture Model for the Wenchuan Earthquake (Mw 7.9), Eastern Tibetan Plateau, China. Bulletin of the Seismological Society of America, 100(5B), 2590–2614, doi: 10.1785/0120090255.

Yuan, R.M., Tang, C.L., Hu, J.C., Xu, X.W., 2014. Mechanism of the Donghekou landslide triggered by the 2008 Wenchuan Earthquake revealed by discrete element modeling. Natural Hazards and Earth System Sciences 14, 1195–1205.

Zhang, L.M., Xu, Y., Huang, R.Q., Chang, D.S., 2011. Particle flow and segregation in a giant landslide event triggered by the 2008 Wenchuan earthquake, Sichuan, China. Natural Hazards and Earth System Science 11, 1153–1162.

Zhang, Y.B., Chen, G.Q., Zheng, L., Li, Y.G., Wu, J., 2013. Effects of near-fault seismic loadings on run-out of large-scale landslide: A case study. Engineering Geology 166, 216–236.

Zhang, Y.B., Wang, J.M., Xu, Q., Chen, G.Q., Zhao, J.X., Zheng, L., Han, Z., Yu, P.C., 2015. DDA validation of the mobility of earthquake-induced landslides. Engineering Geology 194, 38–51.

Zhou, J.W., Cui, P., Hao, M.H., 2016. Comprehensive analyses of the initiation and entrainment processes of the 2000 Yigong catastrophic landslide in Tibet, China. Landslides 13(1), 39–54.

Zhou, J.W., Cui, P., Yang, X.G., 2013. Dynamic process analysis for the initiation and movement of the Donghekou landslide-debris flow triggered by the Wenchuan earthquake. Journal of Asian Earth Sciences 76, 70–84.

Figures:

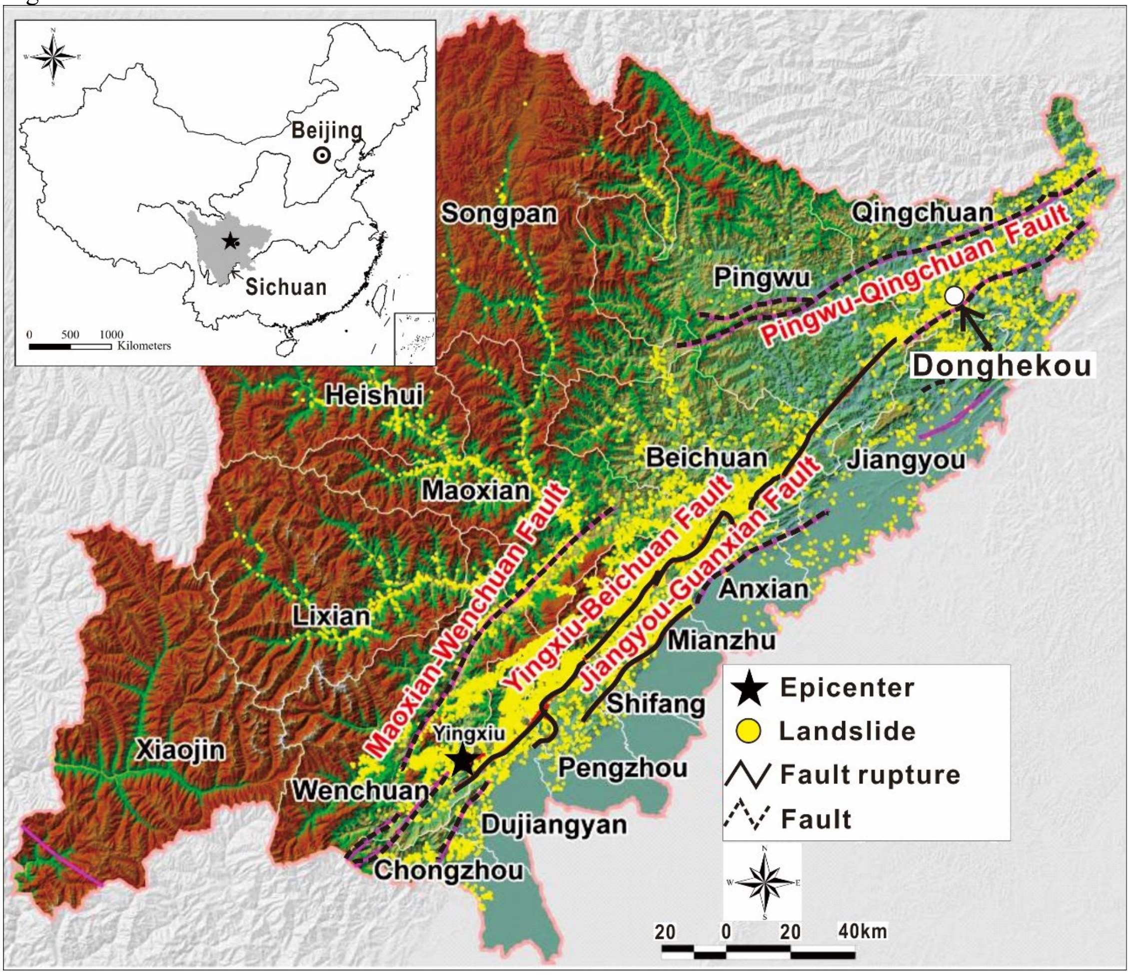

Fig. 1. Epicenter of Sichuan earthquake, distribution of landslides, and location of Donghekou landslide (after Huang, 2009).

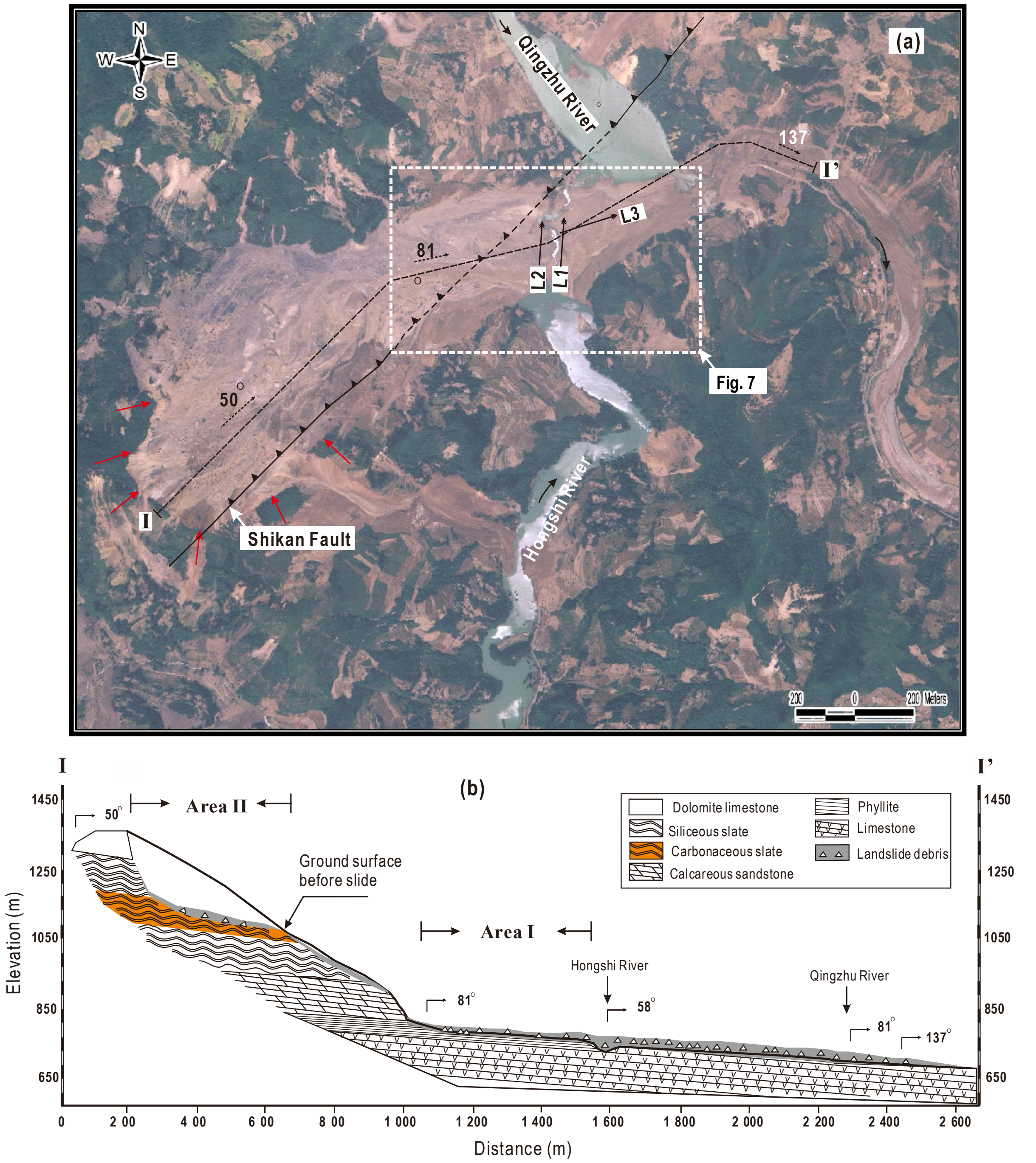

Fig. 2. Donghekou landslide: (a) oblique aerial view; (b) Longitudinal section along the main sliding path (after Yin, 2008). L1, L2, L3: S-wave survey lines presented in Wang et al. (2014), and the arrows in L1~L3 present the extending direction of the survey lines.

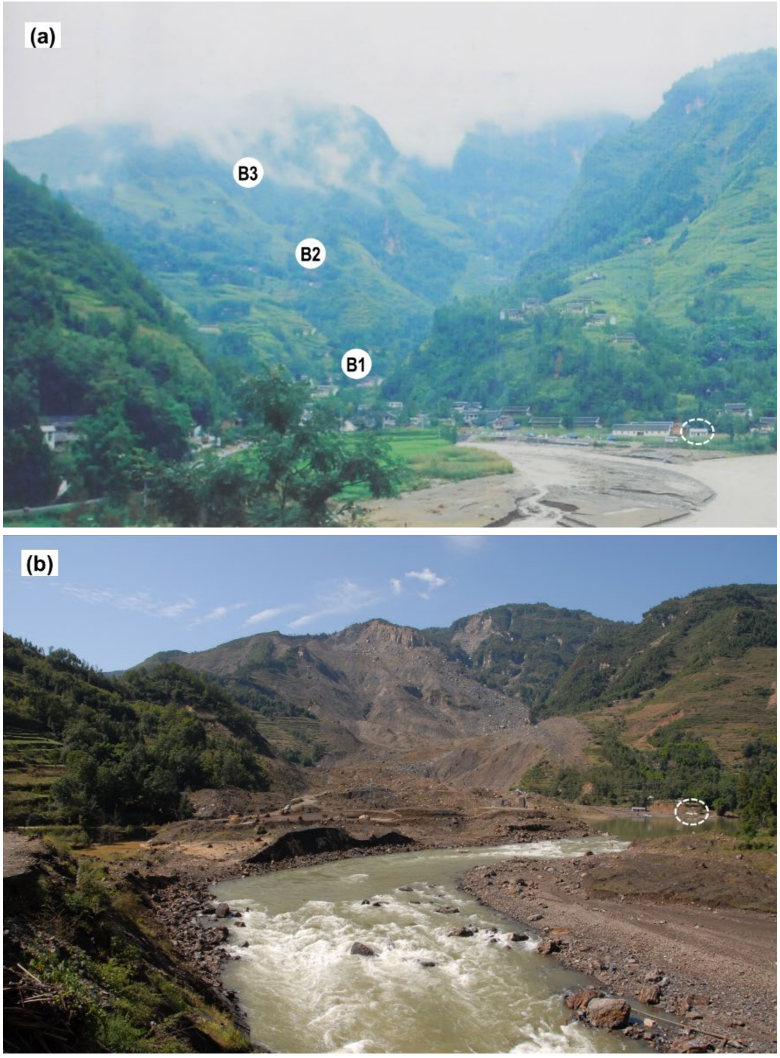

Fig. 3. Views of Donghekou area towards S-W before (a) and after (b) the earthquake, respectively (after Wang et al., 2014). B1: toe part of the valley where the material started to move almost at the same time as the earthquake. B2: location of middle slope; B3: main source area. Photo in (b) was taken on 7 July 2018. The dashed cycles in both views mark the location of a one-stored building that was not destroyed during the earthquake.

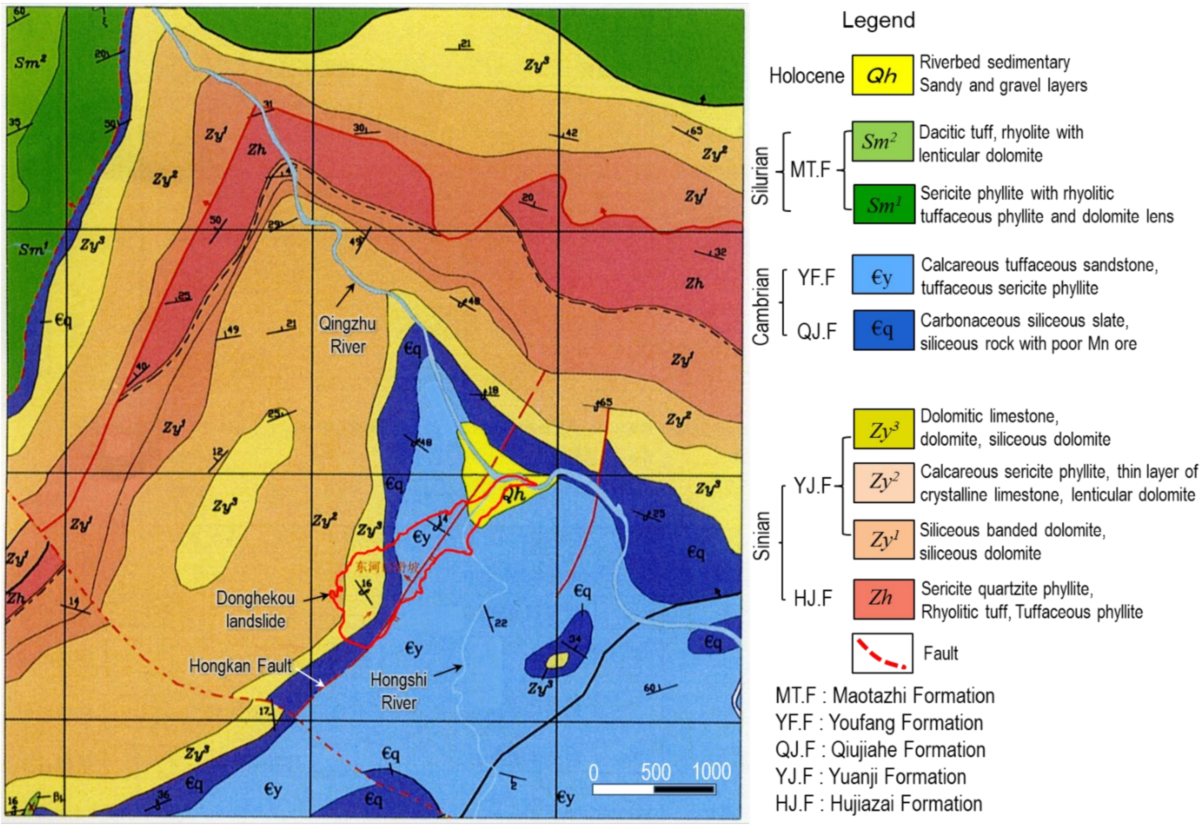

Fig. 4. Geological map of Donghekou landslide area (after Xu and Tang, 2009)

Fig. 5. Fumes rising from the landslide deposits near location B1 in Fig. 3a (taken on March 6, 2009)

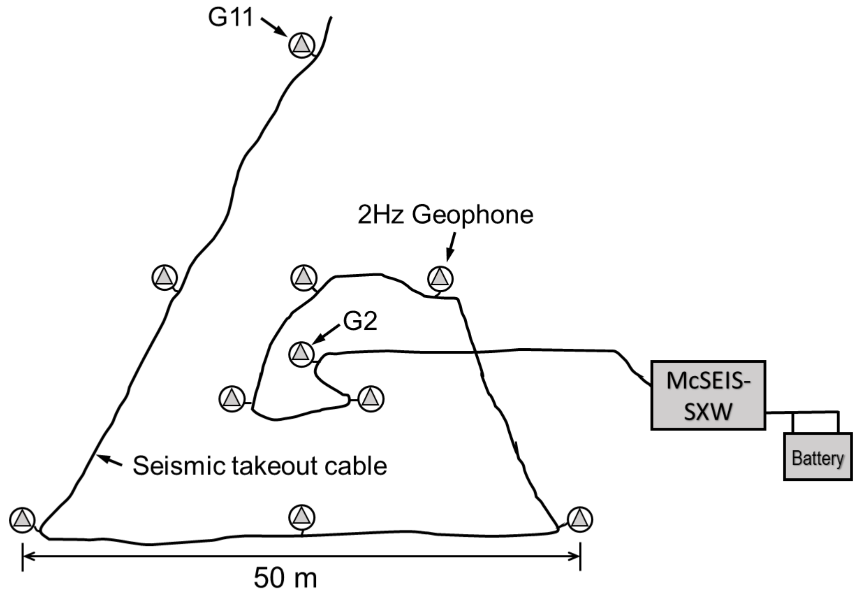

Fig. 6. Layout of geophones in triangular array for microtremor method (passive SPAC method).

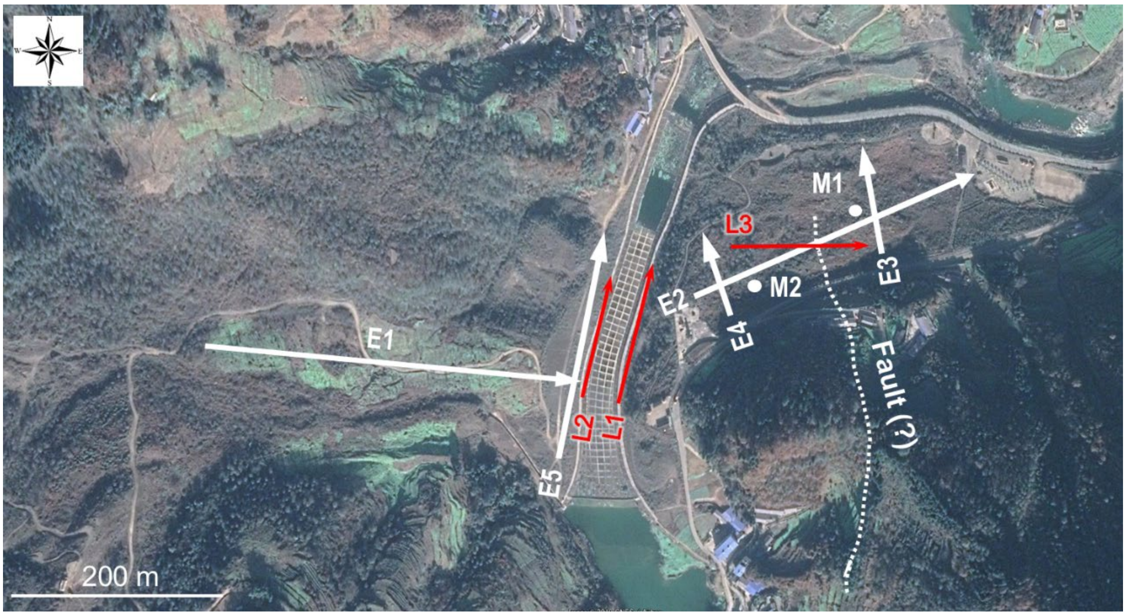

Fig. 7. layout of ERT lines (E1-E5), S-wave survey lines (L1, L2, L3), and locations of microtremor monitoring (M1, M2) (Google Earth image shot on October 30, 2019).

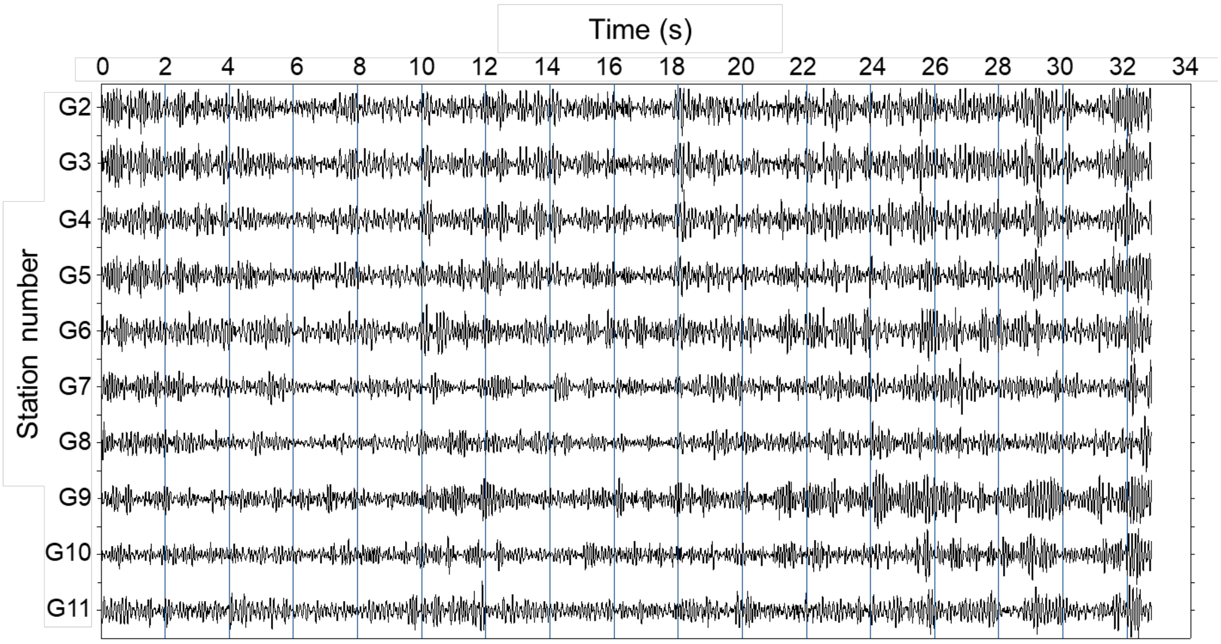

Fig. 8. An example of the record of passive MASW measurement at survey point M2.

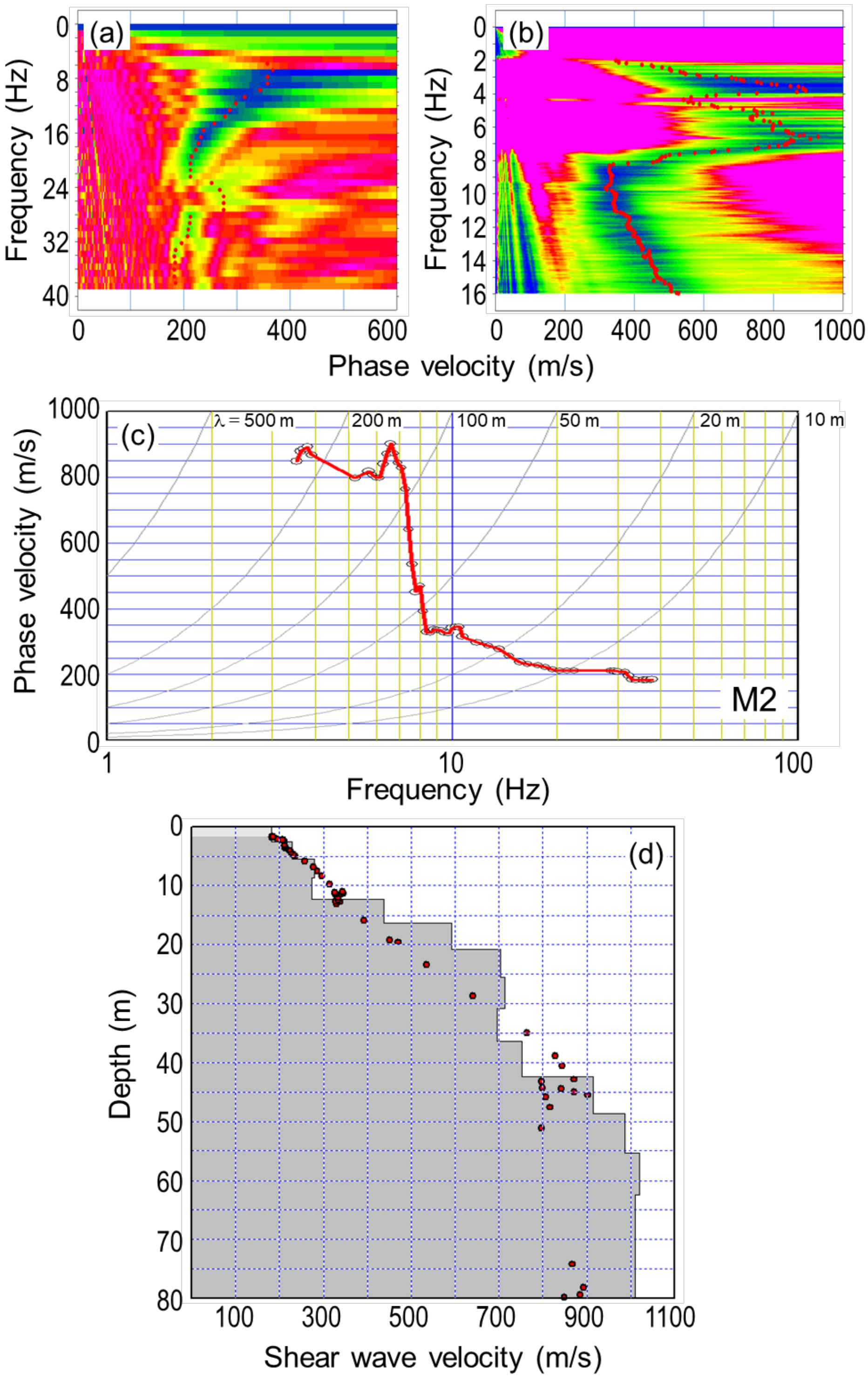

Fig. 9. Vs profile for Point M2. (a), (b) Phase-velocity images in frequency domain obtained by active and passive methods, respectively; red dots indicate the picked phase-velocity; (c) Dispersion curve obtained from (a) and (b); (d) Inverted shear-wave velocity (V_s) profile together with the original picked phase velocities (presented by red points) whose depths were estimated following the one-third-wavelength approximation.

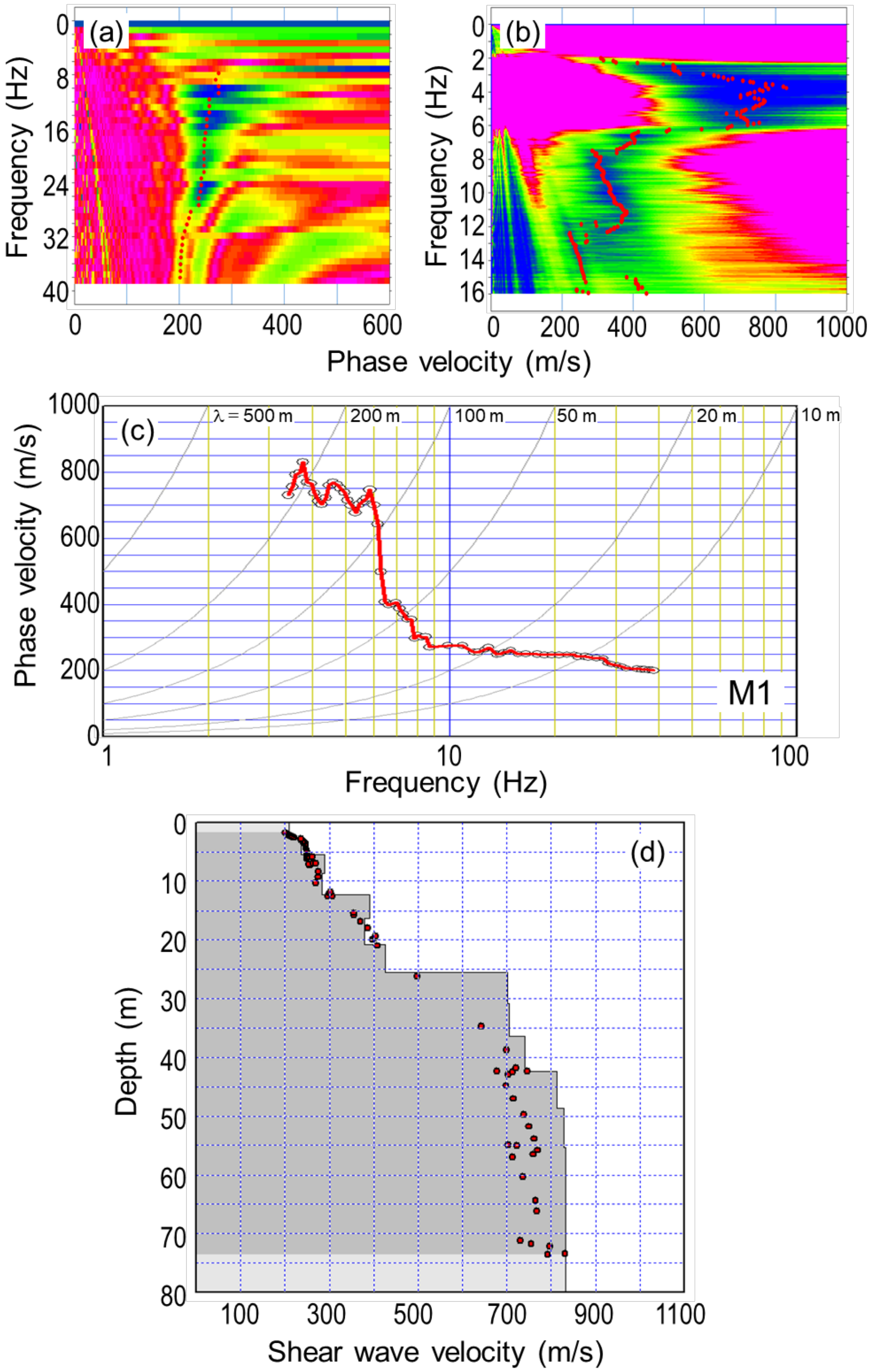

Fig. 10. Vs profile for Point M1. (a), (b) Phase-velocity images in frequency domain obtained by active and passive methods, respectively, there the red dots indicate the picked phase-velocity; (c) Dispersion curve obtained from (a) and (b); (d) Inverted shear-wave velocity (V_s) profile together with the original picked phase velocities (presented by red points) whose depths were estimated following the one-third-wavelength approximation.

.

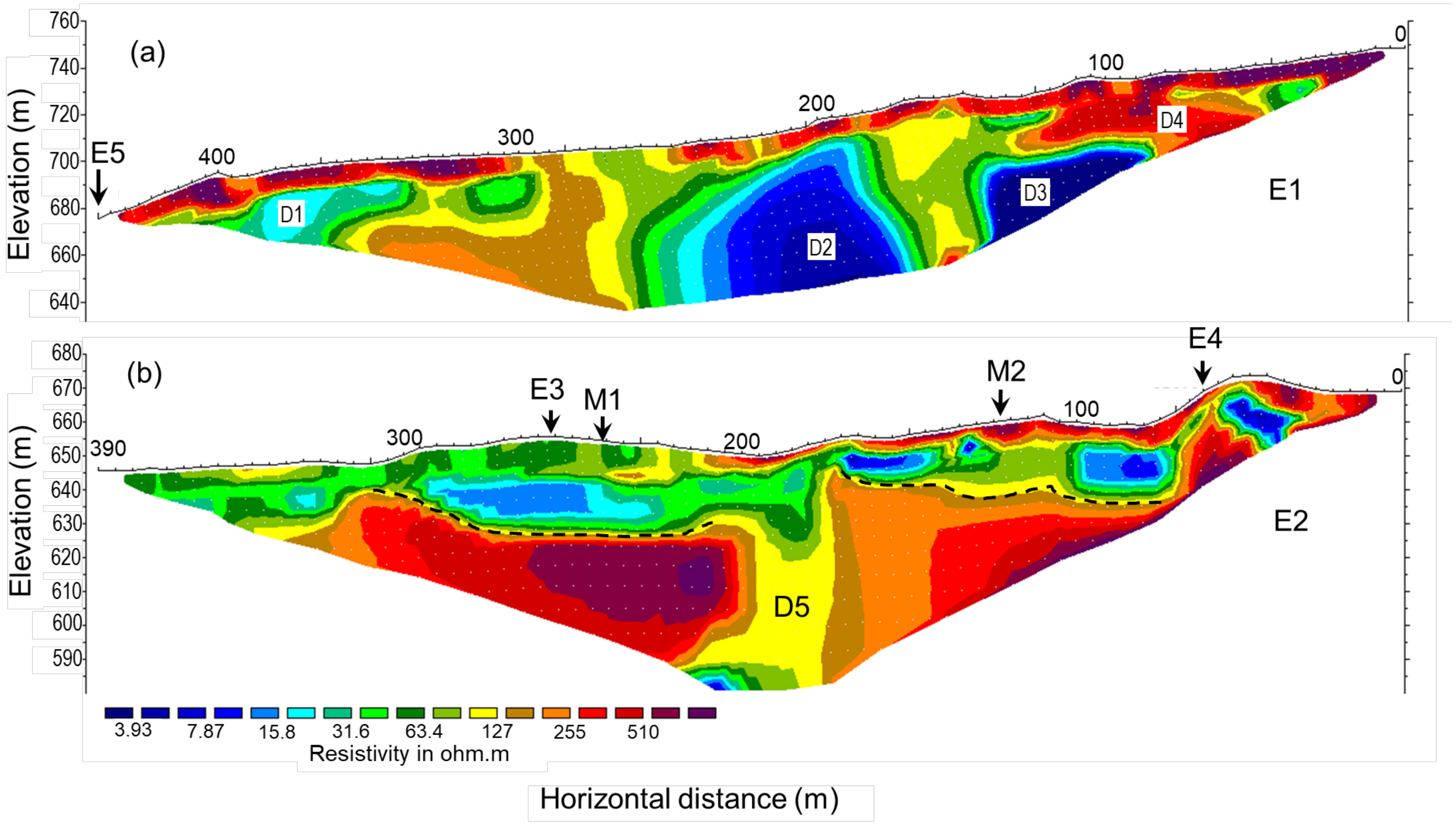

Fig. 11. Electrical resistivity topography (ERT) profiles along survey lines E1 and E2; the locations of cross section survey lines E3-E4 and microtremor measurement sites M1 and M2 are marked.

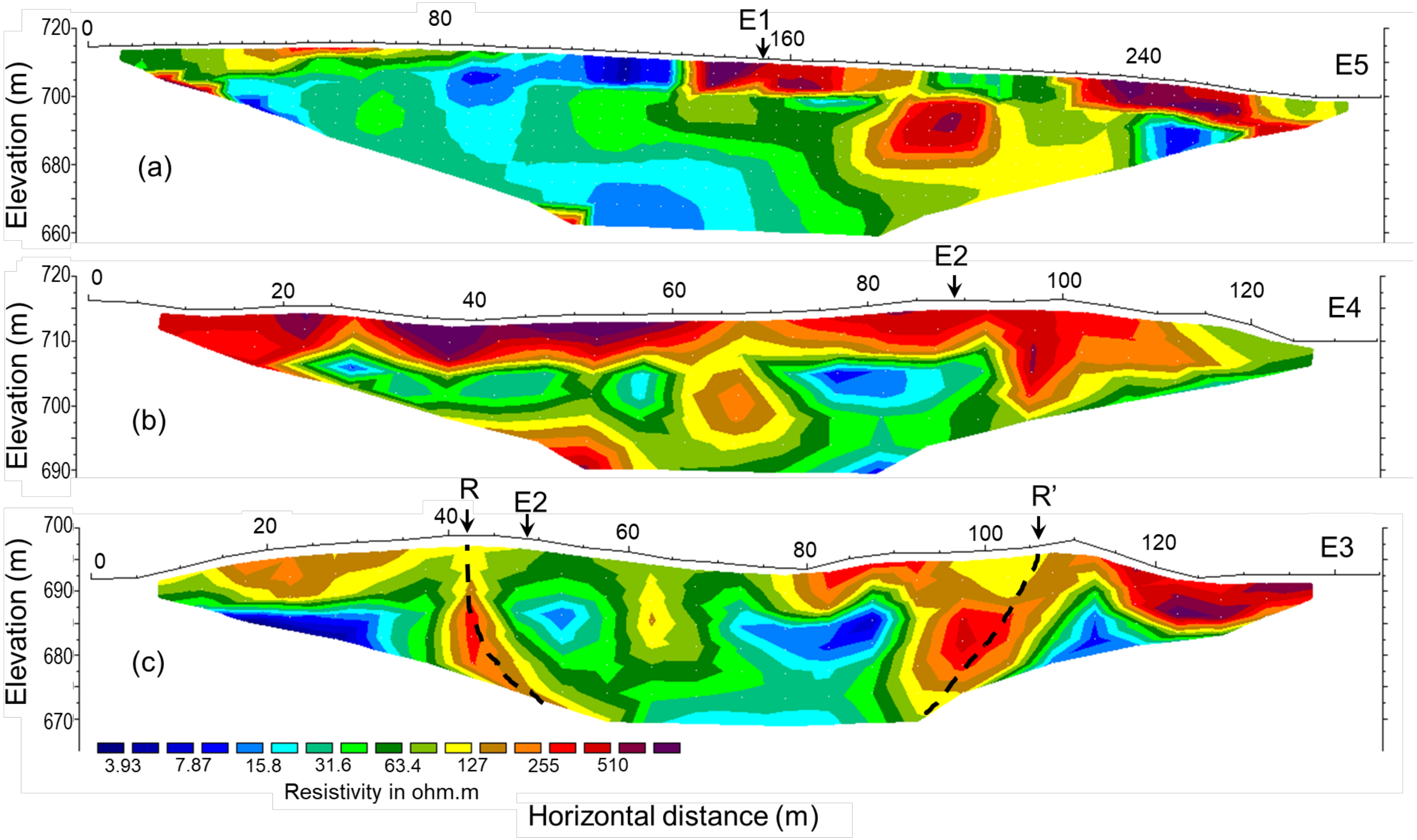

Fig. 12. Electrical resistivity tomography (ERT) profiles along survey line E5 (a), E4 (b), and E3 (c) on the landslide deposits. The arrow shows the location of intersection of two survey lines. Dashed lines mark the boundaries of channelized sliding.

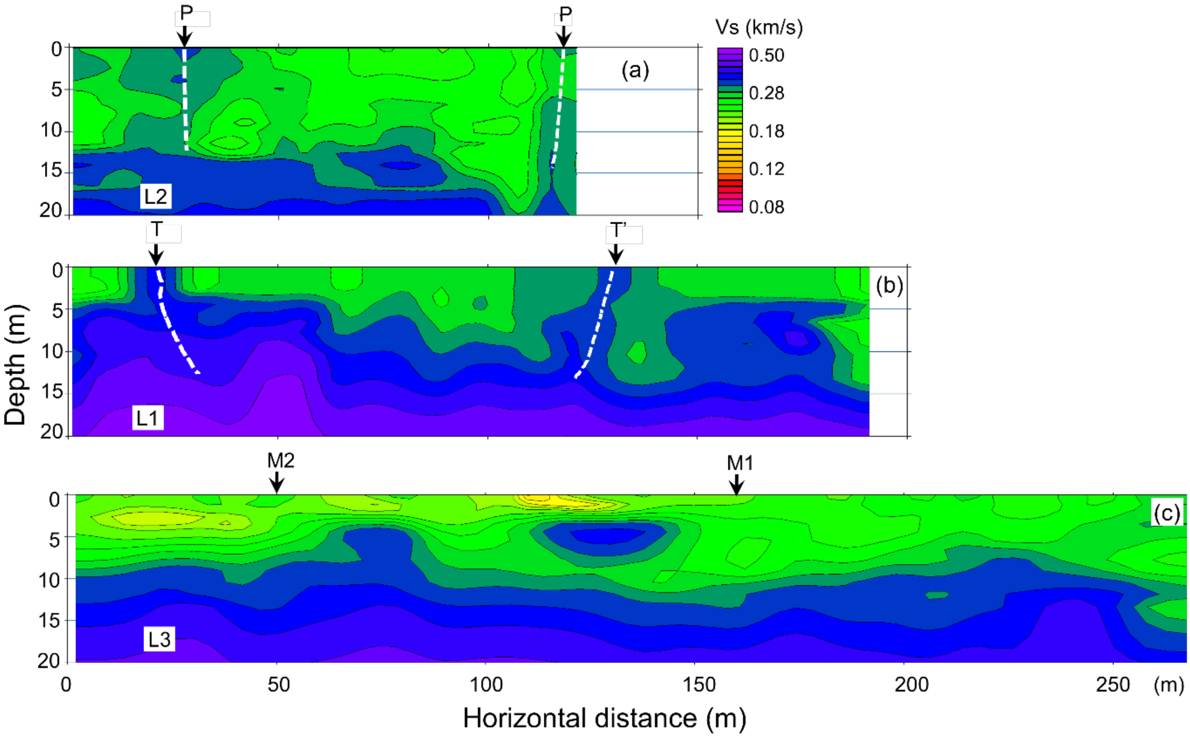

Fig. 13. Shear-wave velocity (Vs) profiles along traverse line L2 (a), L1 (b), and L3 (c), respectively (After Wang et al., 2014).

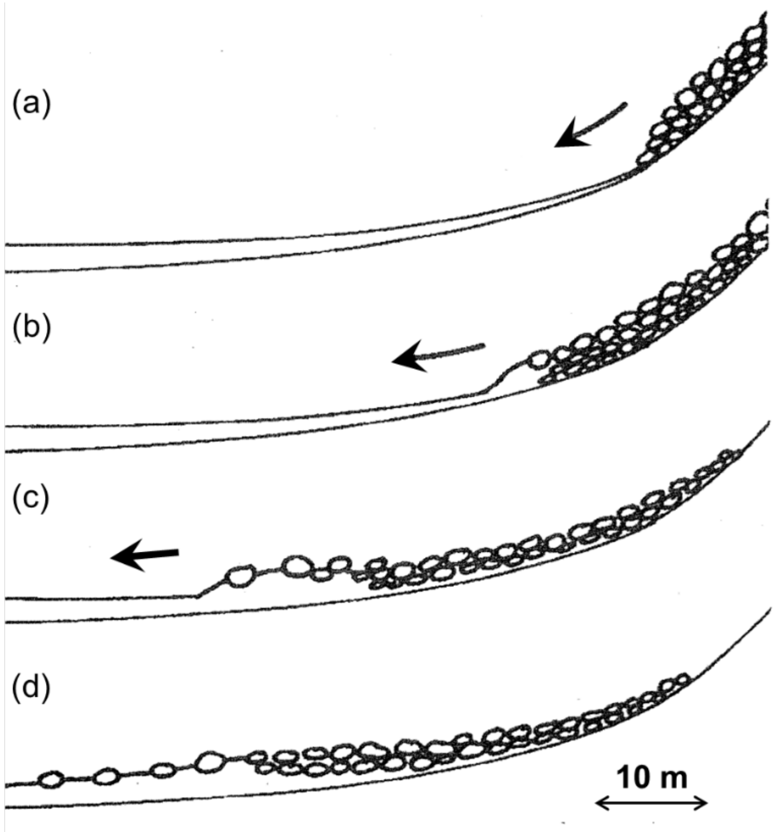

Fig. 14. Schematic illustration of interaction between moving rock mass and liquefiable substrate (after Hungr and Evans, 2004). (a) rock mass moving towards the substrate layer; (b) deformed substrate with overriding rock mass; (c) mud wave projected forward, (d) mud wave and rock mass deposit.

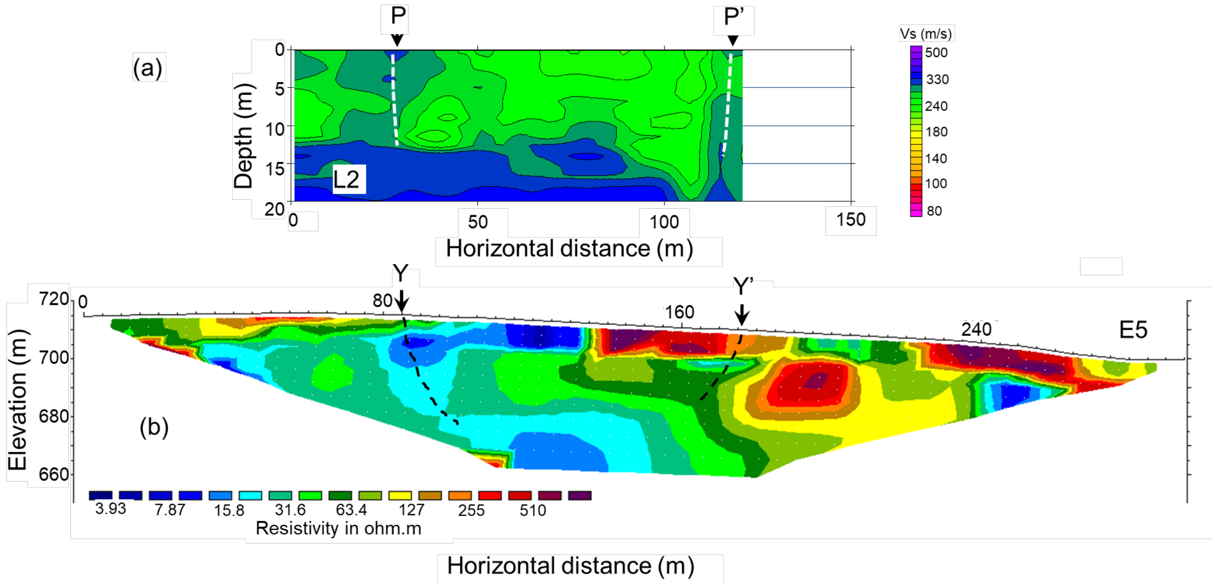

Fig. 15. Comparison between the shear-wave velocity (V_s) profile along L2 (after Wang et al., 2014) and electrical resistivity tomography (ERT) profile along E5. Dashed lines mark the possible boundaries of channelized sliding.

Captions:

Fig. 1. Epicenter of Sichuan earthquake, distribution of landslides, and location of Donghekou landslide (after Huang, 2009).

Fig. 2. Donghekou landslide: (a) oblique aerial view; (b) Longitudinal section along the main sliding path (after Yin, 2008). L1, L2, L3: S-wave survey lines presented in Wang et al. (2014), and the arrows in L1~L3 present the extending direction of the survey lines.

Fig. 3. Views of Donghekou area towards S-W before (a) and after (b) the earthquake, respectively (after Wang et al., 2014). B1: toe part of the valley where the material started to move almost at the same time as the earthquake. B2: location of middle slope; B3: main source area. Photo in (b) was taken on 7 July 2018. The dashed cycles in both views mark the location of a one-stored building that was not destroyed during the earthquake.

Fig. 4. Geological map of Donghekou landslide area (after Xu and Tang, 2009)

Fig. 5. Fumes rising from the landslide deposits near location B1 in Fig. 3a (taken on March 6, 2009)

Fig. 6. Layout of geophones in triangular array for microtremor method (passive SPAC method).

Fig. 7. layout of ERT lines (E1-E5), S-wave survey lines (L1, L2, L3), and locations of microtremor monitoring (M1, M2) (Google Earth image shot on October 30, 2019).

Fig. 8. An example of the record of passive MASW measurement at survey location M2.

Fig. 9. Vs profile for Point M2. (a), (b) Phase-velocity images in frequency domain obtained by active and passive methods, respectively; red dots indicate the picked phase-velocity; (c) Dispersion curve obtained from (a) and (b); (d) Inverted shear-wave velocity (V_s) profile together with the original picked phase velocities (presented by red points) whose depths were estimated following the one-third-wavelength approximation.

Fig. 10. Vs profile for Point M1. (a), (b) Phase-velocity images in frequency domain obtained by active and passive methods, respectively, there the red dots indicate the picked phase-velocity; (c) Dispersion curve obtained from (a) and (b); (d) Inverted shear-wave velocity (V_s) profile together with the original picked phase velocities (presented by red points) whose depths were estimated following the one-third-wavelength approximation.

Fig. 11. Electrical resistivity topography (ERT) profiles along survey lines E1 and E2; the locations of cross section survey lines E3-E4 and microtremor measurement locations M1 and M2 are marked.

Fig. 12. Electrical resistivity tomography (ERT) profiles along survey line E5 (a), E4 (b), and E3 (c) on the landslide deposits. The arrow shows the location of intersection of two survey lines. Dashed lines mark the boundaries of channelized sliding.

Fig. 13. Shear-wave velocity (Vs) profiles along traverse line L2 (a), L1 (b), and L3 (c), respectively (After Wang et al., 2014).

Fig. 14. Schematic illustration of interaction between moving rock mass and liquefiable substrate (after Hungr and Evans, 2004). (a) rock mass moving towards the substrate layer; (b) deformed substrate with overriding rock mass; (c) mud wave projected forward, (d) mud wave and rock mass deposit.

Fig. 15. Comparison between the shear-wave velocity (V_s) profile along L2 (after Wang et al., 2014) and electrical resistivity tomography (ERT) profile along E5. Dashed lines mark the possible boundaries of channelized sliding.